Contents lists available at ScienceDirect

Materials Science & Engineering A

Charpy impact behavior and deformation mechanisms of Cr$_{26}$Mn$_{20}$Fe$_{20}$Co$_{20}$Ni$_{14}$ high-entropy alloy at ambient and cryogenic temperatures

Wei Jiang, Xuzhou Gao, Yang Cao, Yanfang Liu, Qingzhong Mao, Lei Gu, Yonghao Zhao [*]

Nano and Heterogeneous Materials Center, School of Materials Science and Engineering, Nanjing University of Science and Technology, Nanjing, 210094, China

A B S T R A C T

Stacking fault energy (SFE) of high- and medium-entropy alloys (HEAs and MEAs) can be tuned by tailoring the constituent. In this work, we prepared a non-equiatomic Cr$_{26}$Mn$_{20}$Fe$_{20}$Co$_{20}$Ni$_{14}$ HEA with low SFE and investigated the Charpy impact behavior at 298 and 77 K, respectively. The Cr$_{26}$Mn$_{20}$Fe$_{20}$Co$_{20}$Ni$_{14}$ HEA performs an inverse temperature dependence of absorbed impact energy, in contrast to the slight decrease of the equiatomic CrMnFeCoNi HEA. Detailed microstructural investigation along the cracks reveals that dislocation pilling-up and nano-twinning are the dominant strengthening mechanisms for the Cr$_{26}$Mn$_{20}$Fe$_{20}$Co$_{20}$Ni$_{14}$ HEA at 298 K and the CrMnFeCoNi HEA at 298 and 77 K. For Cr$_{26}$Mn$_{20}$Fe$_{20}$Co$_{20}$Ni$_{14}$ HEA at 77 K, except for the enhanced twinning and dislocation storage, additional hexagonal close packed (HCP) structured ε phase transformation also occurred, contributing to the higher strain hardening ability and impact toughness. This study provides experimental evidence for designing HEAs for potential cryogenic applications.

1. Introduction

Seeking for structural materials with high impact and fracture toughness, used in the cryogenic applications, has been a persistent endeavor for the materials community. This is because coupling of low temperature and high impact loading rate poses a huge challenge for selecting applicable materials [1]. It is well known that the body-centered cubic (BCC) metals and alloys usually experience a distinct ductile-to-brittle transition (DBT) and lose most of their toughness with temperature decrease to cryogenic environment [2,3]. Although the DBT is less of a problem in certain face-centered cubic (FCC) metals and alloys (e.g., high Mn TWIP steels), the absorbed impact energy at fracture and impact toughness generally decrease slightly with reduction of temperature [4,5]. Particularly for certain austenite steels (304-type stainless steel [6,7]), the low-temperature deformation induced brittle BCC structured α' martensite usually acts as a crack initiation site near the notch tip region, thereby accelerating the crack propagation and reducing the absorbed impact energy at fracture [8,9]. The corresponding fracture mode performs a transition from ductile and/or partly quasi-cleavage fracture to inter-granular fracture with decreasing temperature from 298 to 77 K [4,8]. On the other hand, an inverse temperature dependence of impact toughness was achieved in the austenite steels (Fe-30Mn-0.11C) by the combined effects of austenite stabilizing elements and an appropriately grain refinement [10].

While developing diluted solid solution alloys, high- and medium-entropy alloys (HEAs and MEAs) containing more than three principal elements in equal or near equal atomic percentages have tremendously broadened the field of alloy design [11-16]. So far, HEAs and MEAs have been reported to possess charming properties, especially at cryogenic temperatures, performing the potential application prospects in cryogenic industries [17,18]. For example, the CrMnFeCoNi HEA [19] and CrCoNi MEA [14] have been reported to possess excellent strength-ductility synergy and high fracture toughness at 77 K, which are ascribed to their low stacking fault energies (SFEs) and a high propensity for twinning. Moreover, the Al$_{0.1}$CoCrFeNi HEA and Al$_{0.3}$CoCrFeNi HEA sustain superior Charpy V-notch impact toughness at cryogenic temperatures, due to the high density of nanoscale twinning [20]. However, an excess of Al content, eg. Al$_{0.75}$CoCrFeNi and Al$_{1.5}$CoCrFeNi, induces numerous brittle BCC phase and ordered B2 compound, accordingly resulting in tremendous reduction of the absorbed energy [21]. Twinning could efficiently dissipate energy and cause dramatic strain hardening by dynamically inducing twin boundaries (TBs) in the plastic region ahead of the V-notch tip, thereby

delaying the formation and propagation of microcracks during the impact deformation [22]. TWIP steels with FCC structure thus serve as cryogenic alloys due to the operative deformation twinning and strain hardening [23]. Besides, dislocation interaction and moderate phase transformation can also contribute to the high strain-hardening capability, thereby enhancing the impact toughness. However, excessive martensite ahead of the crack tip induced by impact load will degrade impact toughness [23-25]. After examining the previous materials with high toughness, we can conclude that homogeneous single-phase FCC structure, high propensity for twinning, high dislocation storage capacity and moderate phase transformation are critical strategies for improving the impact toughness of materials. Our further literature review indicated that the deformation mechanisms (eg. twinning, dislocation and phase transformation) in FCC materials are closely related to SFE, which can be summarized as: (i) dislocation motion when SFEs exceed 60 mJm^{-2}; (ii) twinning when SFEs are in the range of 20–60 mJm^{-2}; and (iii) phase transformation when SFEs are lower than 20 mJm^{-2} [26]. Furthermore, the SFE is also affected by the temperature, and decreases by 20-60% when the temperature decreases from 298 to 77 K [27]. Therefore, controlling the microstructures by tunning the SFE seems to be an applicable option for improving the impact toughness of materials.

In the current work, a non-equiatomic $Cr_{26}Mn_{20}Fe_{20}Co_{20}Ni_{14}$ HEA with low SFE (24 mJm^{-2}) was prepared for the Charpy impact investigation [28,29]. Meanwhile, an equiatomic CrMnFeCoNi HEA with SFE of 30 ± 5 mJm^{-2} was selected for comparison [28,30]. Our early works have demonstrated that the $Cr_{26}Mn_{20}Fe_{20}Co_{20}Ni_{14}$ HEA possessed enhanced strain hardening capacity and ductility, compared with those of other CrMnFeCoNi family alloys [29,31-34]. Therefore, our current research focuses on appraising the capability of $Cr_{26}Mn_{20}Fe_{20}Co_{20}Ni_{14}$ HEA to withstand impact loading and revealing the detailed deformation mechanisms at 298 and 77 K, respectively.

2. Experiments

The studied $Cr_{26}Mn_{20}Fe_{20}Co_{20}Ni_{14}$ (atomic ratios) alloy ingot was prepared with commercially pure elemental metals (Ni, Co: 99.9 wt%; Mn, Fe, Cr: 99.5-99.6 wt%) and was re-melted twice to ensure chemical homogeneity. The ingot was further hot-forged at 1273 K and then annealed at 1273 K for 8 h to achieve a completely recrystallized structure [35]. The CrMnFeCoNi was cold rolled and annealed at 1273 K for 1 h to achieve an equiaxed grained structure.

The Charpy V-notch specimens with the size of $1 \times 4 \times 18$ mm^3, and a V-notch depth of 0.8 mm were prepared from the as-annealed $Cr_{26}Mn_{20}Fe_{20}Co_{20}Ni_{14}$ and CrMnFeCoNi HEAs. An Impact Pendulum Tester (Walter + bai, PH 50/15 J) was used for the Charpy impact tests at room temperature (RT, 298 K) and liquid nitrogen temperature (LNT, 77 K). Traditional Charpy impact tests at LNT generally use ex-situ experiments, in which the samples are precooled first in liquid nitrogen for a period of time, and then taken out for impact in a short time. This gives rise to a problem that the temperature rise of the precooled sample is very rapid, especially when the sample is in contact with the metallic test-piece supports, acting as a good thermal conductor. Besides, the high-speed impact deformation will also lead to obvious temperature rise [34]. Thus, the temperature is not exactly LNT. For acquiring the impact results at precise LNT, a paper device was designed with bottom size similar to the sample, as shown in Fig. 1. First, the device with the sample at the bottom was precooled in liquid nitrogen for about 20 min. Then, impact test was performed on the sample and device with filling of liquid nitrogen, ensuring that the sample was always at the LNT during the impact deformation process. Considering the influence of the paper device, more than 50 impact tests were performed on the individual device at RT and LNT, respectively. The impact energy of the individual device at RT was in the range of 0.016-0.022 J, while that of the individual device filled with liquid nitrogen was in the range of 0.028-0.033 J. Therefore, the actual impact energy of the sample was obtained by the
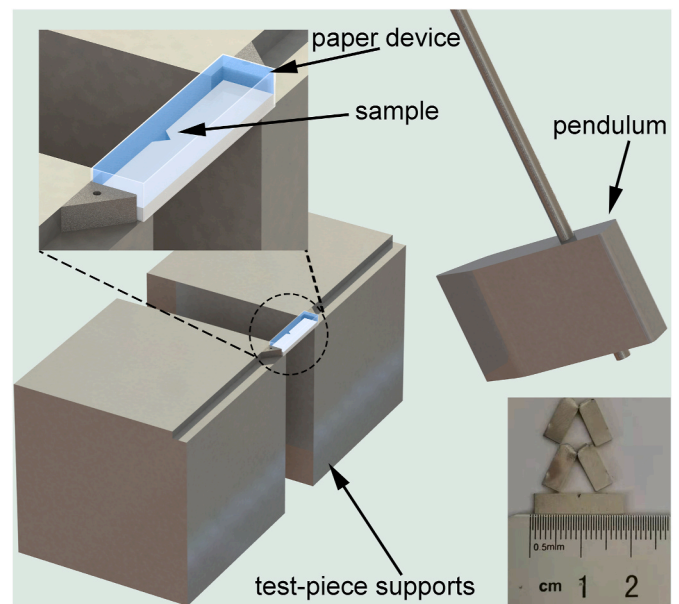

Fig. 1. Schematic diagram of impact test at liquid nitrogen temperature (LNT). The samples lie at the bottom of the paper device filled with liquid nitrogen. Typical impact fractured specimens are shown in the inset.

total energy minus the impact energy of the individual device.

Electron backscatter diffraction (EBSD), scanning electron microscopy (SEM), energy-dispersive spectrometer (EDS) and high-resolution transmission electron microscopy (HRTEM) analyses were performed to analyze the compositions and microstructures of the $Cr_{26}Mn_{20}Fe_{20}Co_{20}Ni_{14}$ and CrMnFeCoNi HEAs. Both EBSD and EDS specimens were electropolished for mirror finish surface in a Buehler ElectroMet 4 polisher. The electrolyte contains 90% acetic acid and 10% perchloric acid and the voltage is 20 V. Specimen foils for HRTEM analysis were prepared by means of focused ion beam (FIB) cutting technology. HRTEM observations were conducted by a Titan G^2 60-300 microscope operated at 300 kV.

3. Results

3.1. Microstructure before Charpy impact

As shown in Fig. 2a, the as-annealed $Cr_{26}Mn_{20}Fe_{20}Co_{20}Ni_{14}$ HEA consists of equiaxed grains with an average grain size of 33 μm, excluding the randomly distributed annealing twins [35]. The composition analysis by the SEM-EDS maps (Fig. 2b) reveals the homogeneous distribution of all the Cr, Mn, Fe, Co and Ni elements within the area of study (500×400 μm^2). The XRD pattern (Fig. 2c) also indicates that the as-annealed $Cr_{26}Mn_{20}Fe_{20}Co_{20}Ni_{14}$ HEA has a single-phase FCC structure. Fig. 3 shows the microstructures of the as-annealed CrMnFeCoNi HEA, which possesses equiaxed grains with a similar grain size of 27.5 μm.

3.2. Charpy impact properties

The absorbed impact energy at fracture and the corresponding impact toughness of the $Cr_{26}Mn_{20}Fe_{20}Co_{20}Ni_{14}$ and CrMnFeCoNi HEAs are illustrated in Fig. 4. As shown in Fig. 4, the absorbed impact energy and impact toughness of the CrMnFeCoNi HEA decrease slightly with reduction of temperature to 77 K. However, the change is so small that it is within the error bar. In contrast, the absorbed energy and impact toughness of the $Cr_{26}Mn_{20}Fe_{20}Co_{20}Ni_{14}$ HEA exhibit an inverse temperature dependence, which increase from 1.75 J to 59.5 Jcm^{-2} at 298 K to 1.89 J and 66.7 Jcm^{-2} at 77 K, respectively.
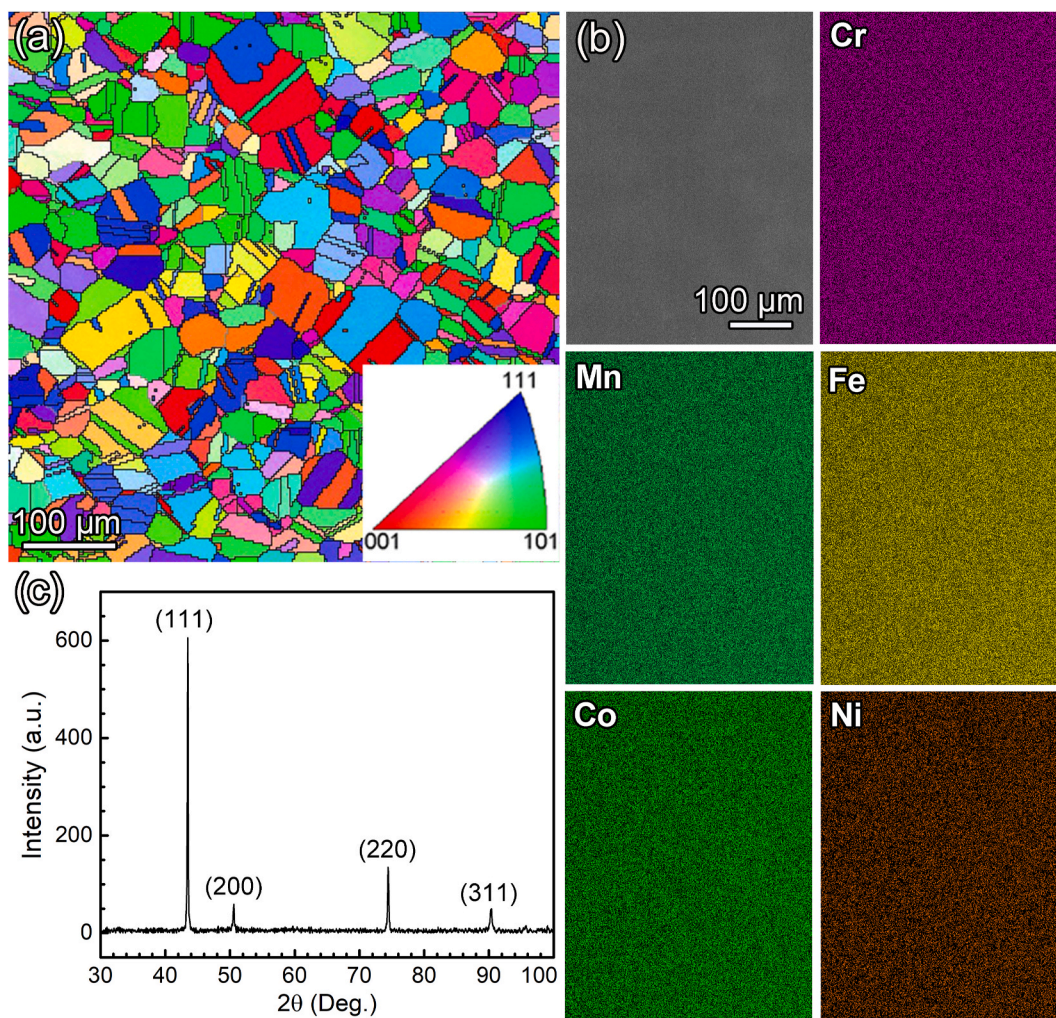
Fig. 2. (a) An EBSD map of the as-annealed $Cr_{26}Mn_{20}Fe_{20}Co_{20}Ni_{14}$ HEA showing fully recrystallized equiaxed grains before the Charpy impact test. The inset is the Inverse Pole Figure color code. (b) SEM-EDS maps of the elements in the $Cr_{26}Mn_{20}Fe_{20}Co_{20}Ni_{14}$ HEA showing homogeneous elemental distributions. (c) The XRD pattern of the $Cr_{26}Mn_{20}Fe_{20}Co_{20}Ni_{14}$ HEA revealing single-phase FCC structure. (For interpretation of the references to color in this figure legend, the reader is referred to the Web version of this article.)
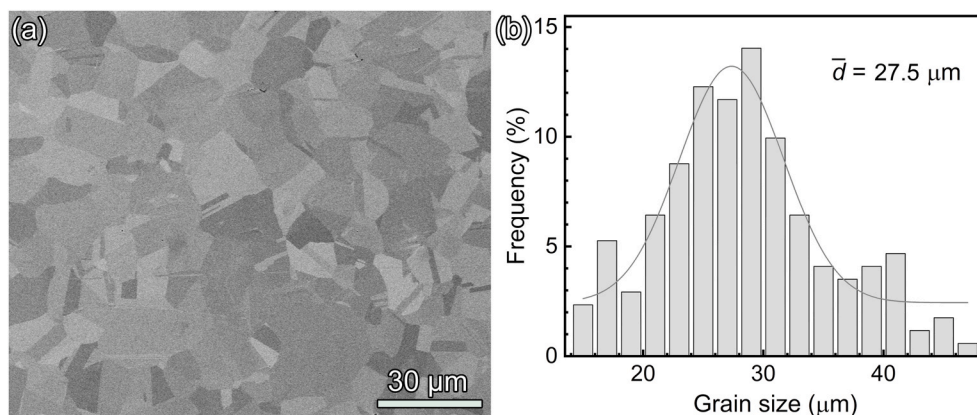

Fig. 3. (a) An SEM image of the as-annealed CrMnFeCoNi HEA showing the microstructures before the Charpy impact test. (b) Grain size distribution.

3.3. Fracture morphologies

To reveal the fracture modes of the $Cr_{26}Mn_{20}Fe_{20}Co_{20}Ni_{14}$ (Cr26) and CrMnFeCoNi (Cantor) HEAs impacted at RT and LNT, respectively, the fracture surface morphologies were examined carefully by using SEM, as shown in Fig. 5. The morphologies of impact fracture surface are divided into the plane strain zone and the shear lip zone. In the plane strain region, numerous dimples are generated, which can achieve high absorbed impact energy and toughness during the impact process [22, 36]. As shown in Fig. 5a, the CrMnFeCoNi HEA shows a higher ratio of
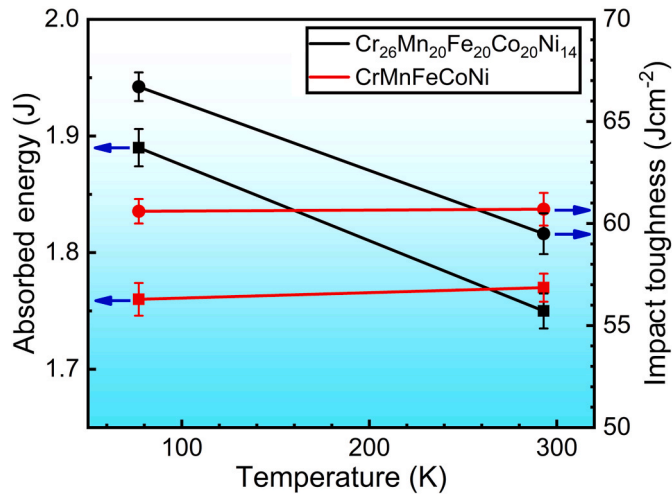
Fig. 4. Comparisons of the $Cr_{26}Mn_{20}Fe_{20}Co_{20}Ni_{14}$ and CrMnFeCoNi HEAs in absorbed energy and impact toughness at 298 and 77 K, respectively.

the plane strain zone at RT, reflected as the larger width of the plane strain area (615 μm). In contrast, the $Cr_{26}Mn_{20}Fe_{20}Co_{20}Ni_{14}$ HEA exhibits the maximum width (664 μm) at LNT, indicating more energy consumed and thus the optimal impact toughness. Fig. 5 b-e show the corresponding magnified fractographs taken from the plane strain zone. Ductile dimples feature the fracture surfaces of all samples tested at RT and LNT. It is worth noting that the samples of $Cr_{26}Mn_{20}Fe_{20}Co_{20}Ni_{14}$ HEA at LNT form denser and smaller dimples (Fig. 5c), which are closely related to the deformation mechanism below.

3.4. Deformation and strengthening mechanisms

Post-mortem EBSD analysis was performed to reveal the deformation and strengthening mechanisms of the $Cr_{26}Mn_{20}Fe_{20}Co_{20}Ni_{14}$ and CrMnFeCoNi HEAs at different temperatures. Fig. 6a shows the longitudinal cross section of the fracture tip of the $Cr_{26}Mn_{20}Fe_{20}Co_{20}Ni_{14}$ HEA sample impacted at 298 K. Region I and II in Fig. 6a were selected for EBSD analysis. The region marked with yellow dotted lines represents the position only rather than the actual area of study. Fig. 6b is the EBSD map of region I which is approximately 400 μm away from the notch. In region I, numerous deformation twins are activated in the grain interiors. The volume fraction (vol%) of twin boundaries in region I is as high as 41 vol%, indicating the twinning is the predominant deformation mechanism due to the low SFE [29,35]. The nano-twin structure is further revealed by the HRTEM image (Fig. 6f) and the corresponding fast Fourier transform (FFT) pattern (Fig. 6g). In addition, massive residual stacking faults (SFs) are observed along the TBs, and two SFs (marked as white arrows) on two conjugated slip planes interact with each other (Fig. 6f). Fig. 6c shows the local misorientation map obtained by misorientation of every EBSD scanning pixel compared with its surrounding pixels. The twinning region has much higher misorientation, i.e. brighter color, than the non-twinning region due to the high density of dislocations accumulated at TBs. According to the formula [37-39]:

$$\rho = \frac{2\theta_{KAM}}{xb} \tag{1}$$

where θ_{KAM} is the kernel average misorientation, x is unit length, which is equal to twice the step size (100 nm) used in EBSD acquisition, $b = 0.253$ nm is the magnitude of Burgers vector and ρ is the dislocation density. The dislocation density around the TBs (marked as ρ_T) is calculated as 6.57×10^{14} m^{-2}, higher than the average value (5.35×10^{14} m^{-2}) of the entire grain (Fig. 9b). The results provide direct evidences for the higher storage capability of dislocation on TBs,

contributing to the high strain hardening ability.

With increasing the distance from the notch (about 2000 μm), slight evolutions of microstructures are observed. As shown in Fig. 6d, massive deformation twins are still observed and the volume fraction of TBs in region II is 36 vol%, lower than that in region I (41 vol%). As shown in Fig. 9b, the average dislocation density of entire grain and around TBs decrease from 5.35×10^{14} to 4.11×10^{14} m^{-2} and 6.57×10^{14} to 4.97×10^{14} m^{-2}, respectively.

With the temperature decrease to 77 K, twinning and dislocation slip are still the dominant deformation mechanisms in $Cr_{26}Mn_{20}Fe_{20}Co_{20}Ni_{14}$ HEA, accompanied with a small number of hexagonal-close packed (HCP) structured ε phase laths. As shown in Fig. 7a, 7b and 7f, the 49 vol% TBs and 9.4 vol% ε phase are observed in region I. In contrast, the microstructures of the CrMnFeCoNi HEA indicate that the twinning is always the dominant strengthening mechanisms at both 298 K and 77 K, just with certain difference in the volume fraction of twins (Figs. 8 and 9a). The HRTEM image (Fig. 7h) further illustrates the microstructures of nano-twins and HCP structured ε phase. Based on the corresponding FFT patterns, the ε phase lamella exhibits a consistent orientation relationship with the FCC matrix as $(000-1)_{HCP} \parallel (-111)_{FCC}$ and $[2-1-10]_{HCP} \parallel [-1-10]_{FCC}$, and shares the same {111} habit planes with the coherent boundaries of the nano-twins. It is noted that debatable BCC structured α' martensite is not observed in $Cr_{26}Mn_{20}Fe_{20}Co_{20}Ni_{14}$ HEA at 77 K. Except the twinning and additional ε phase transforming, the strengthening mechanism of dislocation is also enhanced in the region I at 77 K. According to the local misorientation map (Fig. 7c), the average dislocation density is calculated as 7.06×10^{14} m^{-2}, which is higher than the value (5.35×10^{14} m^{-2}) in the region I at 298 K (Fig. 9b). The results indicate a higher dislocation storage capability and strain hardening ability in $Cr_{26}Mn_{20}Fe_{20}Co_{20}Ni_{14}$ HEA at 77 K.

To further reveal the microstructural evolution with the crack propagation at 77 K, the EBSD characterizations were performed in the region II. As shown in Figs. 7d, **7e** and **7g**, deformation induced twins and ε phases as well as the pilling up of dislocations are still observed, although most of impact energy has been absorbed in the region I. Compared with those in the region I, the volume fraction of TBs and the dislocation density in region II at 77 K decrease sharply from 49 vol% to 44 vol% and from 7.06×10^{14} m^{-2} to 4.69×10^{14} m^{-2} (Fig. 9) respectively. Besides, the volume fraction of ε phase decreases from 9.4 vol% to 5.3 vol%. The decrement might result from weakened impact energy and lowered strain rate in region II.

4. Discussion

4.1. Impacted at RT

For both $Cr_{26}Mn_{20}Fe_{20}Co_{20}Ni_{14}$ and CrMnFeCoNi HEA samples impacted at RT, twinning is the dominant mechanism. Upon impact deformation, deformation twins incessantly generate additional boundaries and directly induce back stress for dislocation slip, particularly for those with slip systems not paralleling to the twin lamellae [40, 41]. The high density of TBs stored by deformation twins efficiently reduce the mean free path of dislocation and increase the interactions between TBs and dislocations, inhibiting the annihilation of dislocations and enhancing the dislocation multiplications [42,43]. Besides, deformation twins have been proved that they additionally inhibit most of the embryonic shear bands to evolve into major ones that could mediate crack propagation [44].

Massive SFs along the TBs induce noticeable strain fields, indicating that stronger forces are necessitated for moving dislocations to across the SFs and twins [35]. Thus, SFs are efficient obstructions for the slip of dislocations, especially for those with slip planes intersecting with the SF plane, thereby substantially contributing to the strain hardening effect [45]. Moreover, the interaction of two SFs on two conjugate slip planes usually forms a super-sessile stair-rod dislocation with a Burgers vector
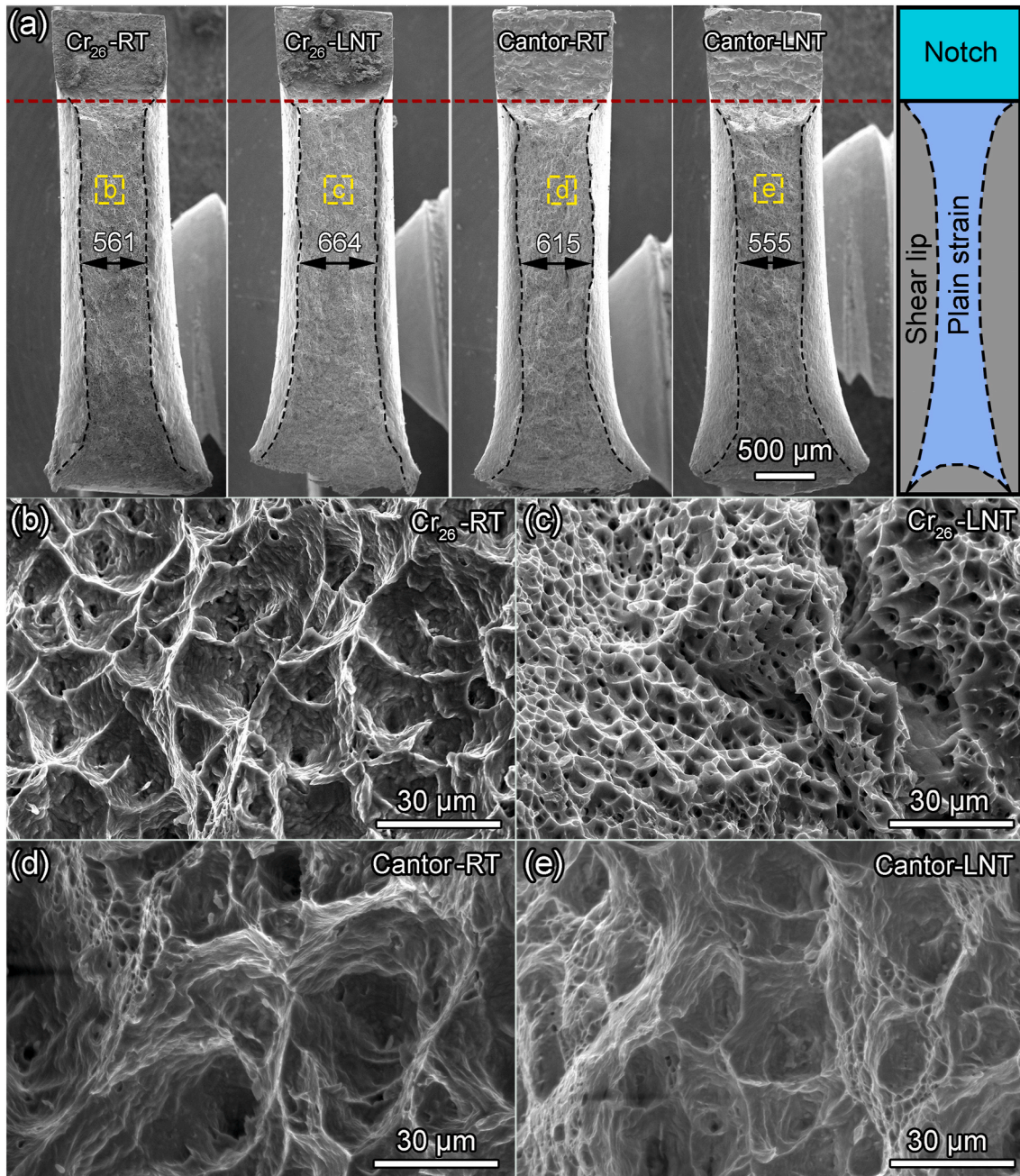
Fig. 5. (a) SEM overviews of the fracture surfaces of the $Cr_{26}Mn_{20}Fe_{20}Co_{20}Ni_{14}$ and CrMnFeCoNi samples. (b) and (c) are SEM images showing the magnified fractographs of the $Cr_{26}Mn_{20}Fe_{20}Co_{20}Ni_{14}$ HEA impacted at RT and LNT, respectively. (d) and (e) are SEM images showing the magnified fractographs of the CrMnFeCoNi HEA impacted at RT and LNT, respectively.

of $1/6<110>$ [29,35]. Such a super-sessile dislocation, also known as Lomer-Cottrell lock, could act as Frank-Read sources for enhancing dislocation multiplication, resulting in strengthening of the $Cr_{26}Mn_{20}Fe_{20}Co_{20}Ni_{14}$ HEA [40].

The density of dislocations and deformation twins in impacted $Cr_{26}Mn_{20}Fe_{20}Co_{20}Ni_{14}$ HEA are closely related to the distance to the notch (Fig. 6). The impact energy is absorbed firstly at the tip of notch, i. e. region I, by activating high density of twins and dislocations. With the crack propagation, the impact energy attenuates gradually and the strain rate decreases, leading to fewer deformation twins and dislocations in the region II. These results indicate that twinning and TB-dislocation interaction under the dynamic loading promote the absorption of the impact energy and retard crack propagation.

4.2. Impacted at LNT

In quasi-static tensile tests, the CrMnFeCoNi HEAs usually show superior combination of strength and ductility with temperature decrease, which are ascribed to the earlier start of twinning at cryogenic temperatures [46,47]. While in Charpy impact tests, the CrMnFeCoNi HEA exhibits slightly decrease as the service temperature decreasing. Low temperature leads to enhanced yield strength of the CrMnFeCoNi HEA, accordingly inducing a reduction of the plastic zone size at LNT [44]. While low temperature enhances the twinning induced hardening ability (higher density of deformation twins), the effective volumes experiencing strain hardening decreases with temperature decreasing. The counterbalance results in the slight decrease of impact toughness of the CrMnFeCoNi HEA at LNT.
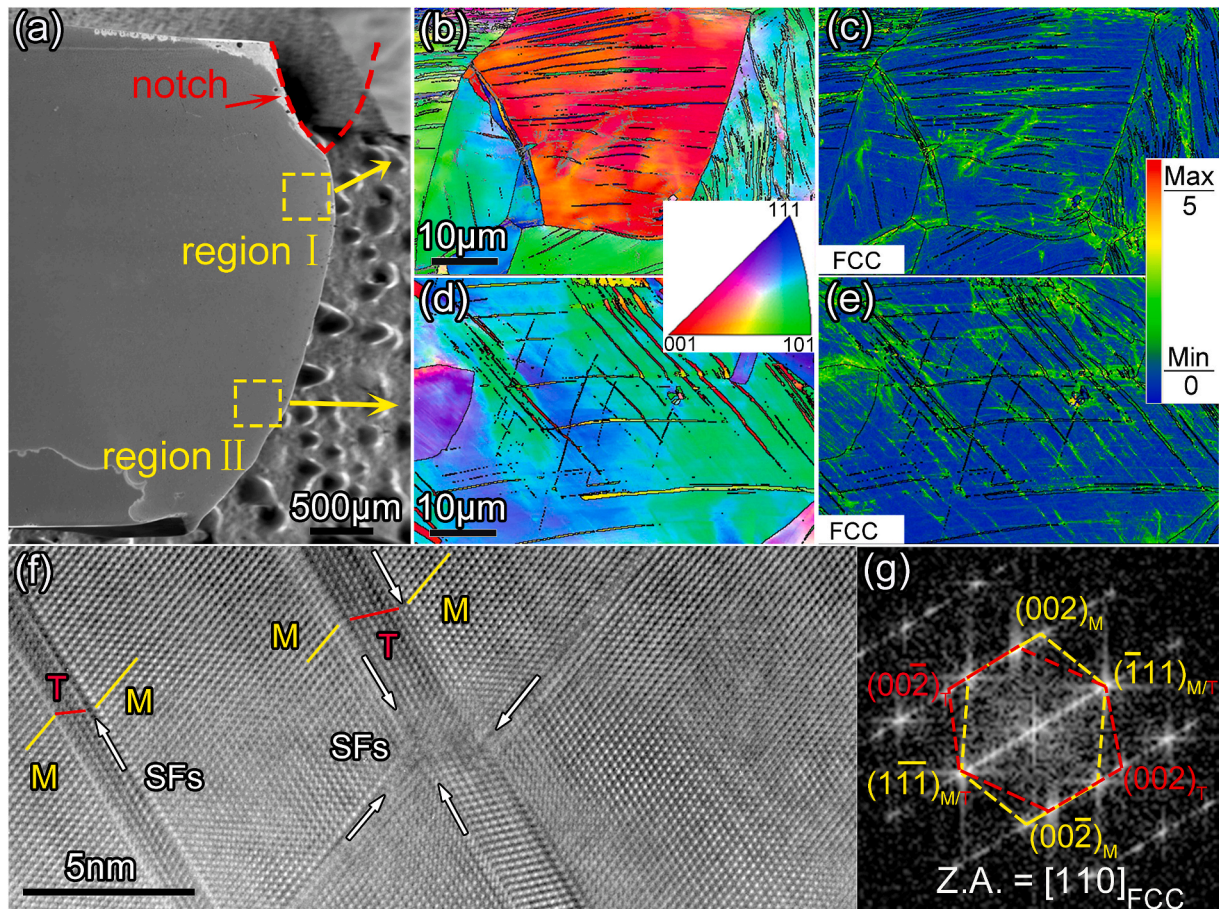
Fig. 6. (a) An SEM image of the $Cr_{26}Mn_{20}Fe_{20}Co_{20}Ni_{14}$ HEA sample impacted at 298 K showing the longitudinal cross-section of the impact-fracture tip; (b) An EBSD image taken at region I; (c) A local misorientation map of region I; (d) An EBSD image taken at region II; (e) A local misorientation map of region II; (f) An HRTEM image showing deformation twins and SFs; (Matrix, twin and SFs are marked by "M", "T" and white arrows, respectively). (g) The corresponding fast Fourier transform (FFT) pattern deduced from (f).

The Charpy impact behavior of $Cr_{26}Mn_{20}Fe_{20}Co_{20}Ni_{14}$ HEA is more striking, exhibiting higher impact toughness at LNT. First, the $Cr_{26}Mn_{20}Fe_{20}Co_{20}Ni_{14}$ is a single-phase FCC HEA with homogeneous microstructures (Fig. 2b), in which Mn segregation at grain boundaries is not captured. In the traditional FeMn- and FeMnNi-based steels, apparent Mn segregation is an adverse factor that has been proved to decrease the grain boundary strength and general toughness, especially at cryogenic temperatures [7,48-50]. Second, the decrease of temperature markedly affects dislocation behaviors, which can be concluded as following: (i) reduced thermal activation volume of dislocation slip for plastic deformation, leading to the decrease of mean free path of dislocation slip [34,51]; (ii) increased height of Peierls barrier, i.e., driving stress for dislocations over the Peierls barrier is higher [51]; (iii) suppressed dislocation dynamic recovery due to the weakened thermally-activated cross-slip and climb [52]. As a result, the reduced activation volume and suppressed dislocation dynamic recovery as well as the enhanced Peierls barrier make dislocation slip difficult, increasing the dislocation storage capability and improving the strain hardening ability of the $Cr_{26}Mn_{20}Fe_{20}Co_{20}Ni_{14}$ HEA at 77 K (Fig. 9b).

Besides, moderate phase transformation increases the toughness of $Cr_{26}Mn_{20}Fe_{20}Co_{20}Ni_{14}$ HEA by dissipating a large quantity of plastic energy [23,24]. The low temperature results in the reduction of SFE, thereby reducing the critical shear stress (CRSS) for phase transforming [27,29,53]. Furthermore, the high strain rate (10^3 s^{-1} [54]) in Charpy impact test facilitates the occurrence of phase transformation at LNT, which usually happens at 4.2 K in quasi-static tensile tests [55,56]. Compared with the microstructures at 298 K, additional ε phase by

phase transformation are activated at 77 K, providing an additional transformation toughening effect during the cryogenic impact test. The variation of impact toughness depends on the equilibrium between the dissipated energy and the fracture properties of the new phase [25]. As shown in Fig. 7h, the HCP structured ε phase in $Cr_{26}Mn_{20}Fe_{20}Co_{20}Ni_{14}$ HEA are mainly formed associated with nano-twins, resulting in a composite structure of nano-twin-HCP lamellae. The nano-composite of dual phase with coherent phase boundaries contributes the optimal distributions of strain and stress, and decreases the possibility of damage nucleation due to their elastic compliance. Moreover, the increased phase boundaries might act as strong barriers for the subsequent dislocation slip. This is because the transmission of edge-component of blocked dislocations at phase boundaries into HCP phase requires activated $<c>$ or $<c + a>$ dislocations with a component along [0001] [57]. The $<c>$ or $<c + a>$ dislocation generally exhibits extremely high CRSS in deformation-induced nano-HCP phase, especially at low temperatures [58].

Based on the above observations of the microstructural evolution along crack propagation, it could be concluded that enhanced nano-twinning, dislocation storage and additional HCP structured ε phase transformation are induced in $Cr_{26}Mn_{20}Fe_{20}Co_{20}Ni_{14}$ HEA at 77 K. The multiple deformation mechanisms promote the accumulation of defects and efficient dissipation of imposed impact energy, thereby sustaining the higher strain hardening ability and achieving higher impact toughness. Compared with the combination of dislocation slip and nano-twins in CrMnFeCoNi HEA at 77 K, the additional phase transforming effect might lead to higher strain hardening ability in the
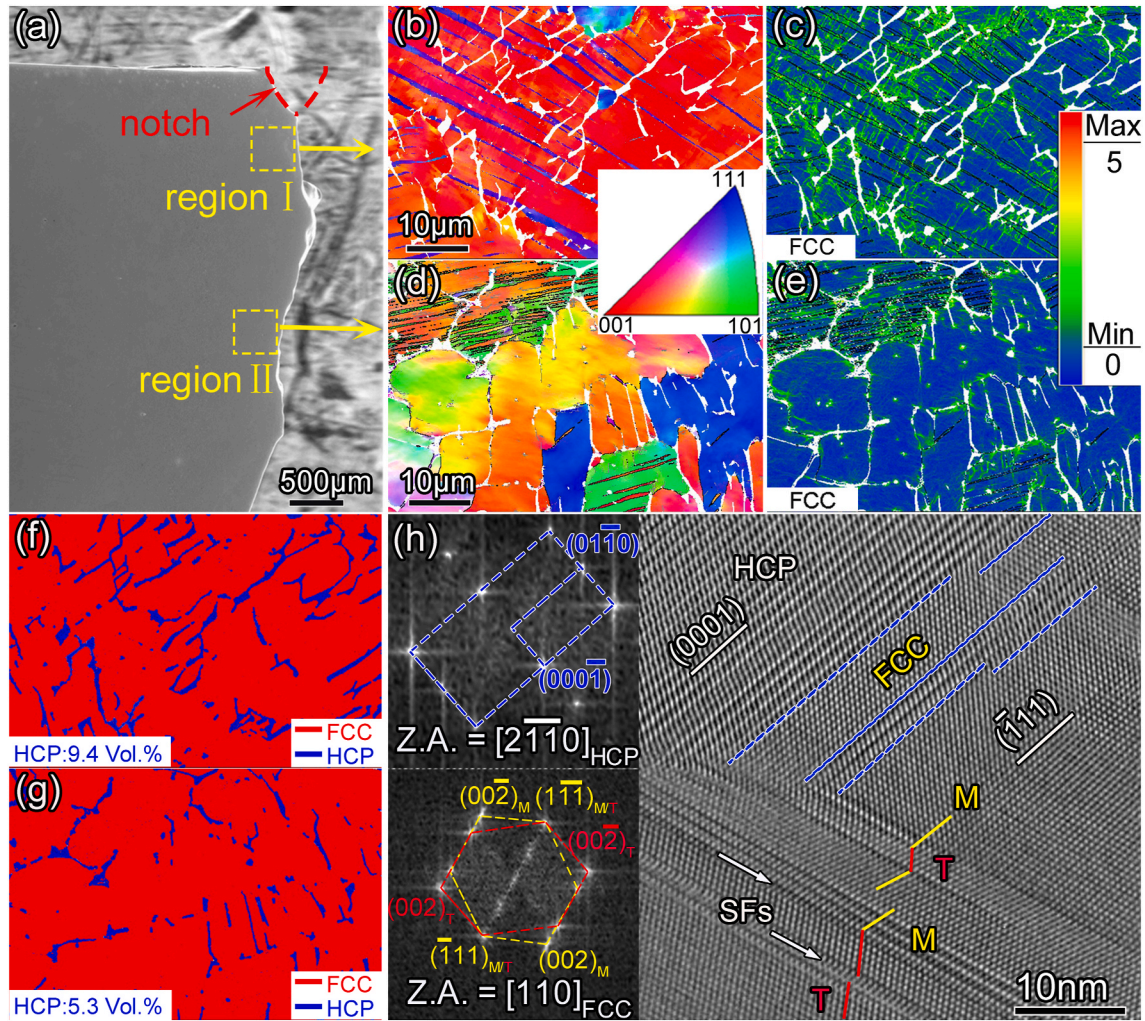
Fig. 7. (a) An SEM image of the $Cr_{26}Mn_{20}Fe_{20}Co_{20}Ni_{14}$ HEA sample impacted at 77 K showing the longitudinal cross-section of the impact-fracture tip; (b) An EBSD image taken at region I; (c) A local misorientation map of region I; (d) An EBSD image taken at region II; (e) A local misorientation map of region II; (f) A phase image of region I; (g) A phase image of region II; (h) An HRTEM image showing deformation twins and HCP phase. Insets are the corresponding FFT patterns indicating the $[2\text{-}1\text{-}10]_{HCP}$ || $[-1\text{-}10]_{FCC}$ relationship. The HCP phase shares the same {111} habit planes with the coherent TBs.

$Cr_{26}Mn_{20}Fe_{20}Co_{20}Ni_{14}$ HEA [21].

5. Conclusions

In this work, fully recrystallized $Cr_{26}Mn_{20}Fe_{20}Co_{20}Ni_{14}$ and CrMnFeCoNi HEAs were prepared and the Charpy V-notch impact tests at RT and LNT were carried out. The EBSD and HRTEM analyses reveal the transition of dominant deformation mechanisms of $Cr_{26}Mn_{20}Fe_{20}$-$Co_{20}Ni_{14}$ from the nano-twinning at 298 K to HCP structured ε phase transformation at 77 K. The cooperation of dislocation pilling-up, SFs intersections, TWIP and/or TRIP effects contributes to an extraordinary impact energy absorption at fracture over a wide temperature range. The main conclusions are as follows:

1. The absorbed energy and impact toughness of the $Cr_{26}Mn_{20}Fe_{20}$-$Co_{20}Ni_{14}$ HEA are 1.75 J and 59.5 Jcm^{-2} at 298 K, respectively. With the temperature decrease to 77 K, the impact parameters increase to 1.89 J and 66.7 Jcm^{-2}, respectively.
2. At 298 K, the post-deformation analyses reveal that high volume fraction nano-twins are activated, acting as the prominent strengthen mechanism. The high density of nano-twins increases the storage capability of dislocation and strain hardening ability, contributing to the high impact toughness. In addition, the volume fraction of TBs

and dislocation density decrease with increase of the distance from the notch, due to the gradually weakened impact energy.
3. With the temperature decrease to 77 K, enhanced nano-twinning and dislocation pilling-up as well as the additional HCP structured ε phase transformation are induced in the $Cr_{26}Mn_{20}Fe_{20}Co_{20}Ni_{14}$ HEA. The multiple deformation mechanisms dissipate imposed impact energy more efficiently, and provide superior strain hardening ability to delay the crack propagation, contributing an extraordinary impact toughness at cryogenic temperature.

To sum up, the non-equiatomic $Cr_{26}Mn_{20}Fe_{20}Co_{20}Ni_{14}$ HEA possesses outstanding impact resistance at room temperature and cryogenic temperature in comparison with the equiatomic CrMnFeCoNi HEA. The fundamental idea is that tuning the SFEs of HEAs by tailoring the atomic proportions of individual components to enhance TWIP and/or TRIP effects, thus to impede dislocation slip and increase dislocation storage for enhancing strain hardening. This discovery provides guidance for designing single phase HEAs with outstanding impact resistance.

CRediT authorship contribution statement

Wei Jiang: Data curation, Visualization, Writing – original draft. **Xuzhou Gao:** Visualization, Investigation. **Yang Cao:** Writing – review
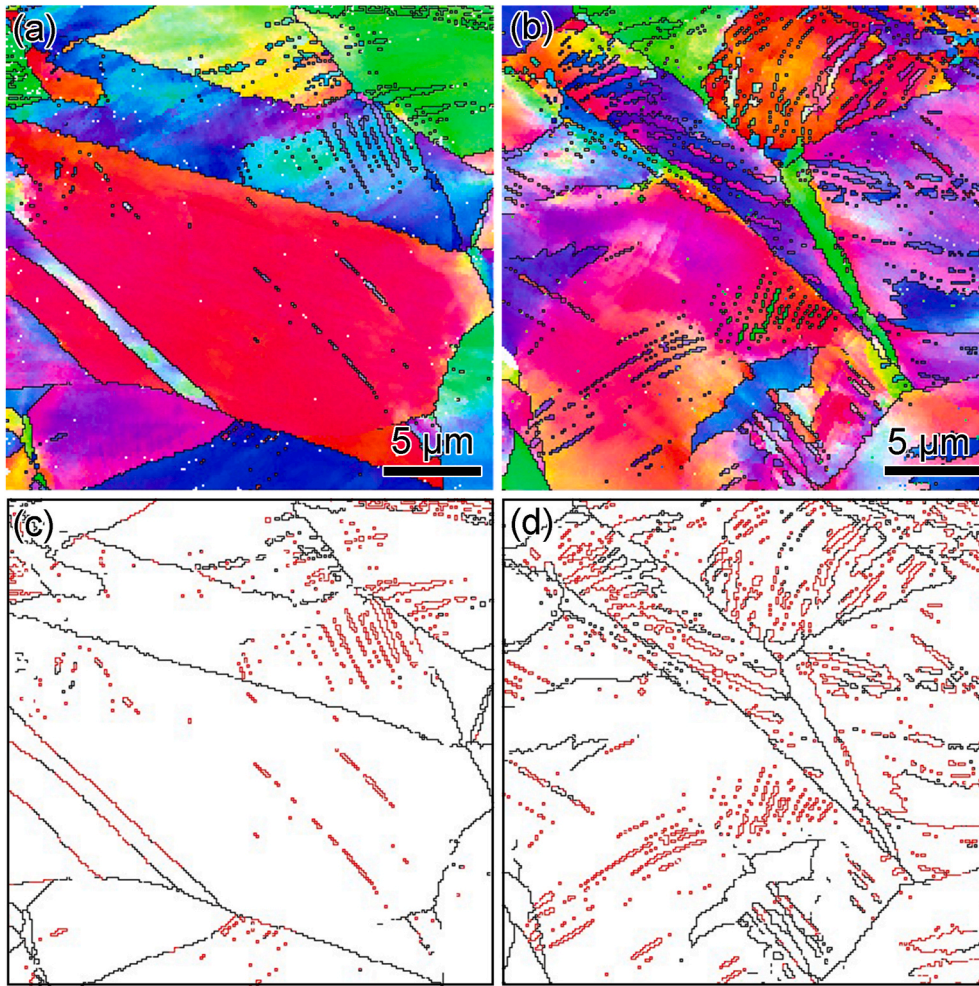
Fig. 8. EBSD images and twin boundary distribution of the CrMnFeCoNi HEA after the Charpy impact test. (a) and (c) at 298 K. (b) and (d) at 77 K.
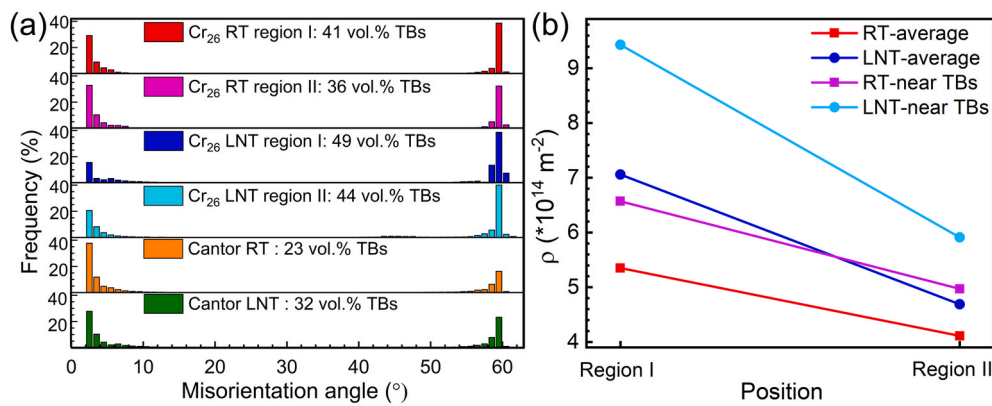

Fig. 9. (a) The distribution of misorientation in the $Cr_{26}Mn_{20}Fe_{20}Co_{20}Ni_{14}$ HEA with different regions and the CrMnFeCoNi HEA impacted at 298 and 77 K, respectively. (b) The dislocation density ρ in different regions of the $Cr_{26}Mn_{20}Fe_{20}Co_{20}Ni_{14}$ HEA impacted at 298 and 77 K, respectively.

& editing, Funding acquisition. **Yanfang Liu:** Investigation, Validation. **Qingzhong Mao:** Investigation. **Lei Gu:** Investigation. **Yonghao Zhao:** Conceptualization, Supervision, Writing – review & editing, Funding acquisition.

Declaration of competing interest

The authors declare that they have no known competing financial interests or personal relationships that could have appeared to influence the work reported in this paper.

References

[1] P. Gao, Z.H. Ma, J. Gu, S. Ni, T. Suo, Y.L. Li, M. Song, Y.W. Mai, X.Z. Liao, Exceptional high-strain-rate tensile mechanical properties in a CrCoNi medium-entropy alloy, Sci. China Mater. (2021), https://doi.org/10.1007/s40843-021-1798-6.

[2] Y. Kimura, T. Inoue, F.X. Yin, K. Tsuzaki, Inverse temperature dependence of toughness in an ultrafine grain-structure steel, Science 320 (2008) 1057–1060.

[3] C.W. Yang, T.S. Lui, L.H. Chen, H.E. Hung, Tensile mechanical properties and failure behaviors with the ductile-to-brittle transition of the α+β-type Mg–Li–Al–Zn alloy, Scripta Mater. 61 (2009) 1141–1144.

[4] J. Han, A.K. da Silva, D. Raabe, S.M. Lee, Y.K. Lee, S.I. Lee, B. Hwang, The effects of prior austenite grain boundaries and microstructural morphology on the impact toughness of intercritically annealed medium Mn steel, Acta Mater. 122 (2017) 199–206.

[5] O. Grässel, L. Krüger, G. Frommeyer, L.W. Meyer, High strength Fe–Mn–(Al, Si) TRIP/TWIP steels development — properties — application, Int. J. Plast. 16 (2000) 1391–1409.

[6] M. Nasim, B.C. Edwards, E.A. Wilson, A study of grain boundary embrittlement in an Fe–8%Mn alloy, Mater. Sci. Eng. 281 (2000) 56–67.

[7] K.H. Kwon, I.C. Yi, Y. Ha, K.K. Um, J.K. Choi, K. Hono, K. Oh-ishi, N.J. Kim, Origin of intergranular fracture in martensitic 8Mn steel at cryogenic temperatures, Scripta Mater. 69 (2013) 420–423.

[8] S.S. Sohn, S. Hong, J. Lee, B.C. Suh, S.K. Kim, B.J. Lee, N.J. Kim, S. Lee, Effects of Mn and Al contents on cryogenic-temperature tensile and Charpy impact properties in four austenitic high-Mn steels, Acta Mater. 100 (2015) 39–52.

[9] O.H. Ibrahim, I.S. Ibrahim, T.A.F. Khalifa, Impact behavior of different stainless steel weldments at low temperatures, Eng. Fail. Anal. 17 (2010) 1069–1076.

[10] Y.H. Wang, Y.B. Zhang, A. Godfrey, J.M. Kang, Y. Peng, T.S. Wang, N. Hansen, X.X. Huang, Cryogenic toughness in a low-cost austenitic steel, Commun. Mater. 2 (2021).

[11] J.W. Yeh, S.K. Chen, S.J. Lin, J.Y. Gan, T.S. Chin, T.T. Shun, C.H. Tsau, S.Y. Chang, Nanostructured high-entropy alloys with multiple principal elements: novel alloy design concepts and outcomes, Adv. Eng. Mater. 6 (2004) 299–303.

[12] B. Cantor, I.T.H. Chang, P. Knight, A.J.B. Vincent, Microstructural development in equiatomic multicomponent alloys, Mater. Sci. Eng. 375–377 (2004) 213–218.

[13] Q.Q. Ding, Y. Zhang, X. Chen, X.Q. Fu, D.K. Chen, S.J. Chen, L. Gu, F. Wei, H.B. Bei, Y.F. Gao, M.R. Wen, J.X. Li, Z. Zhang, T. Zhu, R.O. Ritchie, Q. Yu, Tuning element distribution, structure and properties by composition in high-entropy alloys, Nature 574 (2019) 223–227.

[14] B. Gludovatz, A. Hohenwarter, K.V.S. Thurston, H. Bei, Z. Wu, E.P. George, R.O. Ritchie, Exceptional damage-tolerance of a medium-entropy alloy CrCoNi at cryogenic temperatures, Nat. Commun. 7 (2016) 10602.

[15] Y. Zhang, T.T. Zuo, Z. Tang, M.C. Gao, K.A. Dahmen, P.K. Liaw, Z.P. Lu, Microstructures and properties of high-entropy alloys, Prog. Mater. Sci. 61 (2014) 1–93.

[16] W. Jiang, S.Y. Yuan, Y. Cao, Y. Zhang, Y.H. Zhao, Mechanical properties and deformation mechanisms of a Ni2Co1Fe1V0.5Mo0.2 medium-entropy alloy at elevated temperatures, Acta Mater. 213 (2021) 116982.

[17] M.H. Tsai, J.W. Yeh, High-entropy alloys: a critical review, Mater. Res. Lett. 2 (2014) 107–123.

[18] C.E. Slone, J. Miao, E.P. George, M.J. Mills, Achieving ultra-high strength and ductility in equiatomic CrCoNi with partially recrystallized microstructures, Acta Mater. 165 (2019) 496–507.

[19] B. Gludovatz, A. Hohenwarter, D. Catoor, E.H. Chang, E.P. George, R.O. Ritchie, A fracture-resistant high-entropy alloy for cryogenic applications, Science 345 (2014) 1153–1158.

[20] D.Y. Li, Y. Zhang, The ultrahigh charpy impact toughness of forged AlxCoCrFeNi high entropy alloys at room and cryogenic temperatures, Intermetallics 70 (2016) 24–28.

[21] S.Q. Xia, M.C. Gao, Y. Zhang, Abnormal temperature dependence of impact toughness in AlxCoCrFeNi system high entropy alloys, Mater. Chem. Phys. 210 (2018) 213–221.

[22] J.S. Li, W.B. Qin, W. Peng, M. Chen, Q.Z. Mao, W. Yue, J.J. Kang, D.Z. Meng, D.S. She, X.B. Zhu, Y.S. Li, Effects of geometric dimension and grain size on impact properties of 316L stainless steel, Mater. Lett. 284 (2021) 128908.

[23] P. Duthil, Material Properties at Low Temperature, Institut de Physique Nucléaire d, Orsay, 2015.

[24] T.S. Byun, T.G. Lach, Mechanical Properties of 304L and 316L Austenitic Stainless Steels after Thermal Aging for 1500 Hours, U.S. Department of Energy, 2016. DEAC05-76RL01830.

[25] M.X. Zhang, P.M. Kelly, Relationship between stress-induced martensitic transformation and impact toughness in low carbon austenitic steels, J. Mater. Sci. 37 (2002) 3603–3613.

[26] V. Shterner, I.B. Timokhina, H. Beladi, On the work-hardening behaviour of a high manganese TWIP steel at different deformation temperatures, Mater. Sci. Eng. 669 (2016) 437–446.

[27] S. Curtze, V.T. Kuokkala, Dependence of tensile deformation behavior of TWIP steels on stacking fault energy, temperature and strain rate, Acta Mater. 58 (2010) 5129–5141.

[28] A.J. Zaddach, C. Niu, C.C. Koch, D.L. Irving, Mechanical properties and stacking fault energies of NiFeCrCoMn high-entropy alloy, JOM (J. Occup. Med.) 65 (2013) 1780–1789.

[29] X.Z. Gao, Y.P. Lu, J.Z. Liu, J. Wang, T.M. Wang, Y.H. Zhao, Extraordinary ductility and strain hardening of Cr26Mn20Fe20Co20Ni14 TWIP high-entropy alloy by cooperative planar slipping and twinning, Materialia 8 (2019) 100485.

[30] N.L. Okamoto, S. Fujimoto, Y. Kambara, M. Kawamura, Z.M.T. Chen, H. Matsunoshita, K. Tanaka, H. Inui, E.P. George, Size effect, critical resolved shear stress, stacking fault energy, and solid solution strengthening in the CrMnFeCoNi high-entropy alloy, Sci. Rep. 6 (2016) 35863.

[31] M.J. Yao, K.G. Pradeep, C.C. Tasan, D. Raabe, A novel, single phase, non-equiatomic FeMnNiCoCr high-entropy alloy with exceptional phase stability and tensile ductility, Scripta Mater. 72–73 (2014) 5–8.

[32] Z.M. Li, K.G. Pradeep, Y. Deng, D. Raabe, C.C. Tasan, Metastable high-entropy dual-phase alloys overcome the strength-ductility trade-off, Nature 534 (2016) 227–230.

[33] Y. Deng, C.C. Tasan, K.G. Pradeep, H. Springer, A. Kostka, D. Raabe, Design of a twinning-induced plasticity high entropy alloy, Acta Mater. 94 (2015) 124–133.

[34] Z.G. Wu, Y.F. Gao, H.B. Bei, Thermal activation mechanisms and Labusch-type strengthening analysis for a family of high-entropy and equiatomic solid-solution alloys, Acta Mater. 120 (2016) 108–119.

[35] W. Jiang, X.Z. Gao, Y.Z. Guo, X. Chen, Y.H. Zhao, Dynamic impact behavior and deformation mechanisms of Cr26Mn20Fe20Co20Ni14 high-entropy alloy, Mater. Sci. Eng. 824 (2021) 141858.

[36] Y. Tomita, Effect of microstructure on plane-strain fracture toughness of aisi 4340 steel, Metall. Trans. A 19 (1988) 2513–2521.

[37] M. Calcagnotto, D. Ponge, E. Demir, D. Raabe, Orientation gradients and geometrically necessary dislocations in ultrafine grained dual-phase steels studied by 2D and 3D EBSD, Mater. Sci. Eng. 527 (2010) 2738–2746.

[38] P.J. Konijnenberg, S. Zaefferer, D. Raabe, Assessment of geometrically necessary dislocation levels derived by 3D EBSD, Acta Mater. 99 (2015) 402–414.

[39] W. Jiang, Y. Cao, Y.D. Jiang, Y.F. Liu, Q.Z. Mao, H. Zhou, X.Z. Liao, Y.H. Zhao, Effects of nanostructural hierarchy on the hardness and thermal stability of an austenitic stainless steel, J. Mater. Res. Technol. 12 (2021) 376–384.

[40] X.D. Xu, P. Liu, Z. Tang, A. Hirata, S.X. Song, T.G. Nieh, P.K. Liaw, C.T. Liu, M.W. Chen, Transmission electron microscopy characterization of dislocation structure in a face-centered cubic high-entropy alloy Al0.1CoCrFeNi, Acta Mater. 144 (2018) 107–115.

[41] L. Lu, X. Chen, X.X. Huang, K. Lu, Revealing the maximum strength in nanotwinned copper, Science 323 (2009) 607–610.

[42] K. Jeong, J.E. Jin, Y.S. Jung, S. Kang, Y.K. Lee, The effects of Si on the mechanical twinning and strain hardening of Fe–18Mn–0.6C twinning-induced plasticity steel, Acta Mater. 61 (2013) 3399–3410.

[43] O. Bouaziz, S. Allain, C. Scott, Effect of grain and twin boundaries on the hardening mechanisms of twinning-induced plasticity steels, Scripta Mater. 58 (2008) 484–487.

[44] M.X. Yang, L.L. Zhou, C. Wang, P. Jiang, F.P. Yuan, E. Ma, X.L. Wu, High impact toughness of CrCoNi medium-entropy alloy at liquid-helium temperature, Scripta Mater. 172 (2019) 66–71.

[45] U.F. Kocks, H. Mecking, Physics and phenomenology of strain hardening: the FCC case, Prog. Mater. Sci. 48 (2003) 171–273.

[46] G. Laplanche, A. Kostka, O.M. Horst, G. Eggeler, E.P. George, Microstructure evolution and critical stress for twinning in the CrMnFeCoNi high-entropy alloy, Acta Mater. 118 (2016) 152–163.

[47] F. Otto, A. Dlouhý, C. Somsen, H. Bei, G. Eggeler, E.P. George, The influences of temperature and microstructure on the tensile properties of a CoCrFeMnNi high-entropy alloy, Acta Mater. 61 (2013) 5743–5755.

[48] O. Dmitrieva, D. Ponge, G. Inden, J. Millán, P. Choi, J. Sietsma, D. Raabe, Chemical gradients across phase boundaries between martensite and austenite in steel studied by atom probe tomography and simulation, Acta Mater. 59 (2011) 364–374.

[49] D. Raabe, S. Sandlöbes, J. Millán, D. Ponge, H. Assadi, M. Herbig, P.P. Choi, Segregation engineering enables nanoscale martensite to austenite phase transformation at grain boundaries: a pathway to ductile martensite, Acta Mater. 61 (2013) 6132–6152.

[50] M. Kuzmina, D. Ponge, D. Raabe, Grain boundary segregation engineering and austenite reversion turn embrittlement into toughness: example of a 9wt.% medium Mn steel, Acta Mater. 86 (2015) 182–192.

[51] Z. Wu, H. Bei, G.M. Pharr, E.P. George, Temperature dependence of the mechanical properties of equiatomic solid solution alloys with face-centered cubic crystal structures, Acta Mater. 81 (2014) 428–441.

[52] Y.M. Wang, E. Ma, R.Z. Valiev, Y.T. Zhu, Tough nanostructured metals at cryogenic temperatures, Adv. Mater. 16 (2004) 328–331.

[53] M.A. Meyers, O. Vöhringer, V.A. Lubarda, The onset of twinning in metals: a constitutive description, Acta Mater. 49 (2001) 4025–4039.

[54] T. Lin, A.G. Evans, R.O. Ritchie, Statistical analysis of cleavage fracture ahead of sharp cracks and rounded notches, Acta Metall. 34 (1986) 2205–2216.

[55] J.P. Liu, X.X. Guo, Q.Y. Lin, Z.B. He, X.H. An, L.F. Li, P.K. Liaw, X.Z. Liao, L.P. Yu, J.P. Lin, L. Xie, J.L. Ren, Y. Zhang, Excellent ductility and serration feature of metastable CoCrFeNi high-entropy alloy at extremely low temperatures, Sci. China Mater. 62 (2019) 853–863.

[56] Q.Y. Lin, J.P. Liu, X.H. An, H. Wang, Y. Zhang, X.Z. Liao, Cryogenic-deformation-induced phase transformation in an FeCoCrNi high-entropy alloy, Mater. Res. Lett. 6 (2018) 233–243.

[57] J. Miao, C.E. Slone, T.M. Smith, C. Niu, H. Bei, M. Ghazisaeidi, G.M. Pharr, M.J. Mills, The evolution of the deformation substructure in a Ni-Co-Cr equiatomic solid solution alloy, Acta Mater. 132 (2017) 35–48.

[58] Y.Q. Bu, Z.M. Li, J.B. Liu, H.T. Wang, D. Raabe, W. Yang, Nonbasal slip systems enable a strong and ductile hexagonal-close-packed high-entropy phase, Phys. Rev. Lett. 122 (2019), 075502.